Journal of Rheology

RESEARCH ARTICLE | OCTOBER 16 2024

Experimental and statistical methods for microrheological characterization of heterogeneity in human respiratory mucus mimics of health and disease progression

Neall Caughman; Micah Papanikolas ; Matthew Markovetz; Ronit Freeman ; David B. Hill ; M. Gregory Forest ; Martin Lysy

J. Rheol. 68, 995–1011 (2024)
https://doi.org/10.1122/8.0000789

Experimental and statistical methods for microrheological characterization of heterogeneity in human respiratory mucus mimics of health and disease progression

Neall Caughman,[1] Micah Papanikolas,[2] Matthew Markovetz,[3] Ronit Freeman,[2] David B. Hill,[3,4,5] M. Gregory Forest,[1,3,5,a)] and Martin Lysy[6,a)]

[1]*Department of Mathematics, UNC Chapel Hill, Chapel Hill, North Carolina 27599-3250*
[2]*Department of Applied Physical Sciences, UNC Chapel Hill, Chapel Hill, North Carolina 27599-3050*
[3]*Marsico Lung Institute, UNC Chapel Hill, Chapel Hill, North Carolina 27599-7248*
[4]*Department of Physics & Astronomy, UNC Chapel Hill, Chapel Hill, North Carolina 27599-3255*
[5]*Department of Biomedical Engineering, UNC Chapel Hill & NC State University, Research Triangle Park, North Carolina 27709*
[6]*Department of Statistics & Actuarial Science, University of Waterloo, Waterloo, Ontario N2L 3G1, Canada*

(Received 8 November 2023; final revision received 4 September 2024; published 16 October 2024)

Abstract

Human respiratory mucus (HRM) is extremely soft, compelling passive microrheology for linear viscoelastic characterization. We focus this study on the use of passive microrheology to characterize HRM *heterogeneity*, a phenomenon in normal HRM that becomes extreme during cystic fibrosis (CF) disease. Specifically, a fraction of the mucin polymers comprising HRM phase-separate into insoluble structures, called *flakes*, dispersed in mucin-depleted solution. We first reconstitute HRM samples to the MUC5B:MUC5AC mucin ratios consistent with normal and CF clinical samples, which we show recapitulate progressive flake formation and heterogeneity. We then employ passive particle tracking with 200 nm and 1 μm diameter beads in each reconstituted sample. To robustly analyze the tracking data, we introduce statistical denoising methods for low signal-to-noise tracking data within flakes, tested and verified using model-generated synthetic data. These statistical methods provide *a fractional Brownian motion classifier of all successfully denoised, tracked beads* in flakes and the dilute solution. *From the ensemble of classifier data, per bead diameter and mucus sample*, we then employ clustering methods to learn and infer *multiple levels of heterogeneity*: (i) tracked bead data within vs. outside flakes and (ii) within-flake data buried within or distinguishable from the experimental noise floor. Simulated data consistent with experimental data (within and outside flakes) are used to explore form(s) of the generalized Stokes–Einstein relation (GSER) that recover the dynamic moduli of homogeneous and heterogeneous truth sets of purely flakelike, dilute solution, and mixture samples. The appropriate form of GSER is applied to experimental data to show (i) *flakes are heterogeneous with gel and sol domains*; (ii) *dilute solutions are heterogeneous with only sol domains*; and (iii) *flake and dilute solution properties vary with probe diameter.* https://doi.org/10.1122/8.0000789

I. INTRODUCTION

The method of passive particle tracking microrheology (PPTM) [1–4] has been applied across a wide range of complex fluids to measure linear dynamic moduli, providing an alternative to macrorheometry especially for soft, fragile matter such as the mucus barriers in the respiratory, gastrointestinal, and female reproductive tracts [5–13]. PPTM provides dynamic moduli across a frequency range set by the reciprocal timescales between tracked positions of the microscope system, replacing frequency sweeps at controlled linear stress or strain settings of macrorheometers. PPTM has been indispensable for linear rheological characterization of biological soft matter sharing two properties: (i) extreme softness, i.e., materials that yield at or below the stress-strain controls of macrorheometers and (ii) insufficient availability of sample volumes for macrorheometers. The use of PPTM to explore linear rheology of human respiratory mucus and their disparities between health and disease has been well documented, likewise motivating new methods for automated tracking and measurement error correction [5–12,14–23].

We first briefly recall the experimental and data-analysis protocols of passive particle-tracking microrheology (PPTM) [1–4]. Microbeads are dispersed in a sample and their *position time series*

$$\{X_j = X(j \cdot \tau), \quad j = 0, 1, \ldots, N\}$$

are extracted using particle-tracking microscopy, where $X(t)$ is the continuous-time trajectory of a given microbead, τ is the *experimental lag time between recorded positions of the microscope*, and $N\tau$ is the *total tracking time*. We enforce uniformity of τ and N for each tracked bead for statistical robustness of data inference. From the time series data, assumed free from experimental noise and tracking errors, one then calculates increment statistics, specifically the time-averaged mean-squared displacement (MSD) of each tracked bead, computed for all lag times $n\tau$,

$$MSD_X(n\tau) = \frac{1}{N-n+1}\sum_{j=0}^{N-n} \left\|X_{n+j} - X_n\right\|^2. \quad (1)$$

a)Authors to whom correspondence should be addressed; electronic mails: forest@unc.edu and mlysy@uwaterloo.ca

Positions X_j have dimension d, typically $d = 2$ with beads tracked in distinct focal planes. These MSD statistics are then inserted into the generalized Stokes–Einstein relation (GSER) [1–4] [Eq. (2)], mapping from increments at lag times $n\tau$ to dynamic moduli at frequencies $\omega = 1/n\tau$. This formalism, as with the Stokes–Einstein relation for viscous fluids, applies to presumed *homogeneous* complex or simple fluids. One performs ensemble averaging of the MSD over all tracked beads, denoted as $\langle MSD_X(n\tau)\rangle$, which is inserted into the GSER (2). $\Im(\cdot)$ denotes the Fourier transform, $G^*(\omega)$ is the complex shear modulus with the real part, the storage modulus $G'(\omega)$, and the imaginary part, the loss modulus $G''(\omega)$,

$$G^*(\omega) = G'(\omega) + iG''(\omega) = \frac{k_B T}{\pi r i\omega \Im(MSD_X(n\tau))}. \quad (2)$$

In *heterogeneous* complex or simple fluids, there is typically no *a priori* knowledge of the lengthscales of heterogeneity, nor where the probe diameter resides within the lengthscale spectrum, nor is there any means to control the sampling of the heterogeneous structure by the probes. Given these limitations, it is not clear what, if anything, ensemble averaging over all tracked beads reflects about the fluid. In the reconstituted HRM samples studied here, we observe highly heterogeneous mobilities of beads (described below in terms of scaling behavior of the *denoised* MSD statistics per bead). Every tracked and successfully denoised bead time series, with 1800 position observations, yields increments across all experimental lagtimes $n\tau$. We find and verify that the denoised $MSD_X(n\tau)$ is extremely well approximated by a *unique, stationary, fractional Brownian motion (fBm) process*. We give detailed support of this statement with experimental tracked bead data and synthetic simulated data in Figs. S4 and S5 of the supplementary material. We illustrate an accurate reconstruction of the empirical MSD by developing a *robust fBm classifier for each tracked and successfully denoised bead.* We provide the fBm classifier for 200 nm and 1 μm diameter beads that are experimentally tracked in each reconstituted HRM sample. *We, therefore, assert that the denoised time series of every tracked bead in each HRM sample provides a robust statistical sampling of the local medium fluctuations imparted to that bead across the experimental timescales of the increment time series. These robust results strongly support that the surrounding medium of each tracked bead is homogeneous over the experimental timescales and lengthscale traversed by the tracked bead.* We are careful to filter out any data from beads that are not isolated (within 2–5 diameters of another bead) to ensure pure single-bead signal data or from beads without full position time series. We then apply the GSER to $MSD_X(n\tau)$ of each tracked bead to get a statistical estimate of the dynamic moduli surrounding that bead,

$$G^*(\omega) = G'(\omega) + iG''(\omega) = \frac{k_B T}{\pi r i\omega \Im(MSD_X(n\tau))}. \quad (3)$$

Below, we illustrate the validity of this and the ensemble-averaged form (2) of GSER using synthetic simulated data consistent with experimentally tracked beads in posited homogeneous samples of HRM. In addition to previously documented increases in mucus concentration [9,12], as noted above, cystic fibrosis (CF) HRM networks progressively reconfigure [17,21] through the formation of dense, raftlike, structures called *flakes* dispersed in the remaining dilute mucin solution. In advanced stages of CF, two clinical observations have been documented: the ratio of the primary mucins MUC5B and MUC5AC changes, while simultaneously a progressive fraction growing to 50% of the mucins MUC5B and MUC5AC become sequestered within flakes that do not swell nor dissolve in the remaining, dilute airway surface salt-water solvent. Advanced CF mucus can, therefore, be described, at a coarse scale, as a two-phase mixture: a dense phase of mucin-rich flakes, and a more dilute phase consisting of the remaining mucins in solvent. Additional scales of spatial heterogeneity potentially exist (and confirmed herein) within the two coarse phases for any given sample: (1) the dilute phase is likely to have a spatially heterogeneous mucin concentration since it has been continuously depleted as mucins stochastically condense and phase separate to form flakes, leaving behind the dilute phase plus encapsulated beads in the local concentration surrounding each bead; (2) the flakes, on the other hand, are the condensates of the mucin phase separation process, likewise encapsulating beads in the local, high mucin concentrations surrounding each bead. We note that lateral flake dimensions are highly variable, observed clinically, and in reconstituted HRM samples, they range from 1 to 100 μm [21]. Unknown free-volume pore-size distributions that govern the mobility of passive probes in reconstituted HRM samples match healthy and two stages of progressive CF clinical samples. The diffusive mobility of beads within flakes is hindered, sometimes sufficiently low to be indistinguishable from immobile beads tracked by the instrumentation, i.e., the tracked bead signal is sometimes entangled in the noise floor. Heterogeneity and lack of control over bead spatial sampling of the dilute and flake phases impose hard constraints on the form of the generalized Stokes–Einstein relation (GSER) one should use. The inherently low bead numbers within flakes give a sparse, local sampling of flake rheology. Ensemble averaging of bead MSDs in the GSER, Eq. (2), is justified by an ergodicity assumption for homogeneous materials: ensemble averaging of bead MSDs in the time domain is equivalent to frequency-domain averaging of the Fourier-transformed MSDs, further assuming sufficient sampling of the material. However, these assumptions are strongly violated for flake-prevalent mucus. To overcome these limitations, we proceed with the following steps:

- *Experimental*: Reconstitute bulk samples of HBE mucus to match the MUC5B:MUC5AC ratio during three progressive stages of CF [24] with 200 nm and 1 μm diameter beads uniformly dispersed at the outset of sample preparation. The beads then undergo unresolved repositioning as the mucins undergo degrees of phase separation, leading to beads encapsulated in dilute and flake phases of each sample and bead diameter. Particle tracking microscopy then records the position time series of all tracked beads

per subsample from the three bulk HRM samples. (The Experimental Methods: Materials and Data Collection section provides more details.)

- *Filtering of the data:* Apply a proximity filter to ensure beads are isolated and not within five diameters of another bead to avoid bead-bead interactions and cross-correlations that are the focus of two-bead microrheology, cf [25–27].
- Given that within-flake beads often have mobilities on the order of the noise floor, *use the denoising procedure* of [18], extended in [28] and here *to analyze low mobility data from beads in flakes.* Explore several classifier metrics of individual bead time series and seek the optimal metric for the experimental data.
- *Use synthetic simulated data* to replicate features of the experimental data, in particular, heterogeneous tracked particle time series, including extremely low mobility and low signal-to-noise-ratio (SNR) as well as moderate to waterlike mobilities and higher SNRs. We then *identify an optimal classifier metric* (described in detail below) that is applied to each tracked bead time series.
- *With the optimal classifier metric, hierarchically cluster the experimental datasets*. First, distinguish beads outside and within flakes. [The accuracy of this automated task is experimentally tested by visual assessment of beads outside and inside flakes, with 209/212 (over 98%) beads correctly identified.] Second, distinguish whether tracked beads within flakes can be confidently disentangled from the noise floor. Third, test whether the ensembles of denoised within-flake and outside-flake beads, per bead diameter and reconstituted sample, are statistically homogeneous. (N.B. All fail the homogeneity test.) Fourth, given that within-flake and outside-flake ensembles are nonhomogeneous, apply a clustering algorithm to the within-flake and outside-flake classifier datasets for the three bulk samples for each bead diameter. Fifth, test homogeneity of all individual clusters containing at least four beads. (N.B. All such clusters fail the homogeneity test.)
- Given nonhomogeneity of each cluster, *apply the GSER to single beads in each cluster and then cluster average in frequency space to infer the dynamic moduli of all denoised data clusters within and outside of flakes, for 200 nm and 1 μm diameter beads. Assess the resulting rheological heterogeneity* between clusters within and outside of flakes, for each probe size.
- *Assess probe lengthscale dependence in the dynamic moduli* from the 200 nm and 1 μm bead diameter results for all three mucin-ratio samples.

II. EXPERIMENTAL METHODS: MATERIALS AND DATA COLLECTION

A. Mucus/mucin model systems

Mucus is harvested from normal human bronchial epithelium (HBE) cell cultures as previously described [24,29,30]. HBE mucus has been shown to be similar to native mucus in both biochemical composition [31,32] and biophysical properties [30]. Briefly, cells are recovered from surgical waste by the UNC Marsico Lung Tissue Procurement Core. Cells are seeded and grown on 1 cm diameter, collagen-coated inserts. After ~6 weeks, cells become confluent, form an air-liquid interface, and begin to produce mucus. Culture lavages are collected twice weekly with 200 μl phosphate buffered saline (PBS) per 1 cm diameter insert. Washings from >100 cultures and >10 donors are pooled to minimize patient-to-patient and insert-to-insert variability.

HBE cultures are also used as a source of MUC5B, while Calu3 cells are the source for MUC5AC. Mucins are purified from dilute culture washings by isopycnic density gradient as previously described [10,33]. Cesium chloride is added to washings to raise the density to 1.35 g/ml, and then loaded into 40 ml centrifugation tubes. These tubes are spun at 40 000 rpm for 60 h, after which the samples are unloaded as 20 fractions. During centrifugation, mucins migrate to the denser part of the tube, while globular proteins migrate to the less dense fractions. Confirmation of mucin-rich fractions is achieved with periodic acid-Shifts reaction to label the heavily glycocholate mucins [33]. Mucin-rich fractions are then pooled and concentrated against absorbent gel following the protocol with HBE washings [29].

B. Mucus flake production

To synthetically produce flakes, mucin solutions are diluted to 2% solids by weight and mixed to contain different ratios of the primary gel-forming mucins, MUC5B and MUC5AC, to ratios observed in HBE mucus from healthy non-CF donors vs. progressive cystic fibrosis. Specifically, we reconstitute mucin solutions with MUC5B:MUC5AC ratios of 90%:10% (non-CF), 80%:20% (mild CF), and 60%:40% (severe CF). From different batches of the same bulk samples, *200 nm and 1 μm carboxylate-modified fluorescent beads (Invitrogen, F8811 or F8823) are mixed with mucins overnight* at 4 °C at 1:10 000 or 1:140 dilution, respectively. Flakes are formed by injecting one of the above 3 mucin solutions (50 μl) into a 4 mM calcium chloride solution (500 μl, Sigma 223506) to mimic the *in vivo* environment, the corresponding solutions are diluted to the concentration of 1.8 mg/ml.

C. Particle tracking microrheology

Diffusive mobility of microspheres incorporated in mucus flakes are imaged by a combination of brightfield microscopy with fluorescent microscopy. Data are collected on a Nikon TE-U 2000 inverted microscope at 40× on a Grasshopper3 USB3 (Teledyne Flir) at 60 frames per second for 30 s, as previously described [10,34]. Once image sequences are collected, they are processed by the TrackPy particle tracking software [35–37] to extract the individual particle trajectories [21,24].

D. Flake visualization

Prior to the collection of image sequences used to generate particle trajectories, a bright field image is collected and overlayed with the first frame of the fluorescent image sequence to confirm if beads are contained within or outside

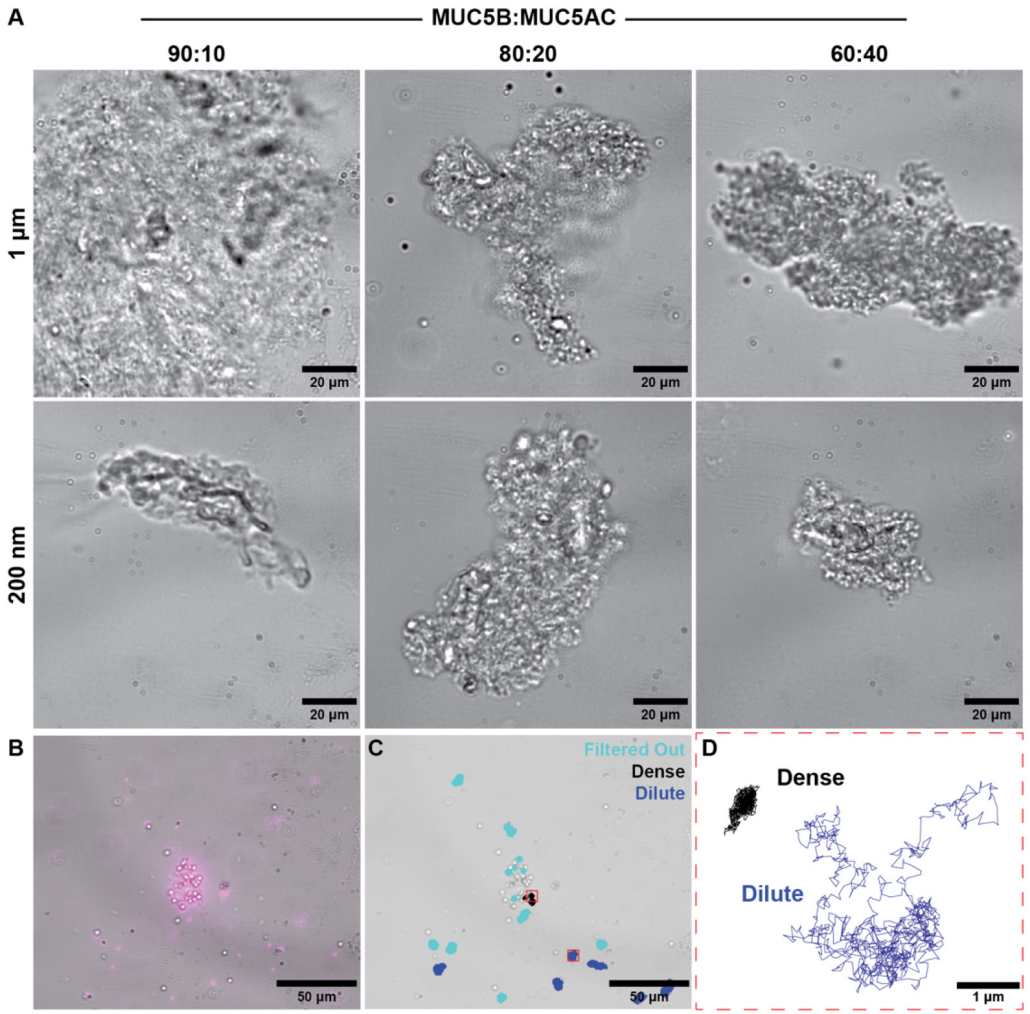

FIG. 1. Experimental images of reconstituted mucus flakes with microbeads. (a) Brightfield images of reconstituted mucus flakes. (b) Overlay with a fluorescent image. (c) Reconstituted mucus flake overlaid with trajectories of tracked beads. (d) Higher resolution of individual trajectories of two tracked beads, one within and one outside of a flake.

flakes in the dilute solution. Some beads are encapsulated within the phase-separated flakes, while others are encapsulated outside the flakes in the dilute solution remaining after the mucins condense to form flakes. Prior to applying the statistical methods described below, all tracked bead time series are first passed through a series of filters; the most notable of which is the proximity filter, which ensures that the only forces acting on the bead are from the medium itself and not from other beads in proximity. A full analysis of the data and details on the prefiltering is provided in the "Data Cleaning" section of the supplementary material.

Figure 1 shows mucosal flakes with individual beads numbered and highlighted, showing vast differences in the flake size as well as the number of beads within different flakes.

Next, we explain the predictor-corrector method for estimating the MSD of tracked beads, and then we analyze data from flake-prevalent mucus samples and discuss the results.

E. Particle position time series data and statistical analysis of the data

Recall Eq. (1) for the MSD per lag time, $n\tau$. For a spherical particle of radius r diffusing in a purely viscous medium, e.g., water or glycerol of viscosity η, the position time series is described by d-dimensional Brownian motion, for which the MSD scales linearly with all lag times,

$$MSD_X(n\tau) = 2dDn\tau, \tag{4}$$

where D is the diffusivity of the medium given by the Stokes–Einstein relation

$$D = \frac{k_B T}{6\pi\eta r}. \tag{5}$$

Soft biological materials like mucus are both viscous and elastic, with different responses at different frequencies of forcing. In viscoelastic materials, the MSD of passive beads is sublinear over the timescales for which the medium exhibits memory due to elastic storage and release. For 200 nm to 1 μm diameter passive beads in respiratory mucus, and for our microscope system, the memory timescales encompass the camera shutter timescale (1/60 s) and the total bead observation time (30 s). Furthermore, *over experimental timescales, each individual tracked bead approximately exhibits a*

subdiffusive MSD power law

$$MSD_X(n\tau) = 2dD_\alpha(n\tau)^\alpha, \quad 0 < \alpha \leq 1, \tag{6}$$

identical to fractional Brownian motion. It is important to emphasize that the statistical classifier for Brownian motion, $\alpha = 1$, is one dimensional, the diffusivity D, whereas for subdiffusive fractional Brownian motion, $0 < \alpha < 1$, the classifier is two dimensional, $(\alpha,\ D_\alpha)$ [17,18]. The power law α reflects the degree of subdiffusivity of the medium surrounding each tracked particle. The prefactor (generalized diffusivity) D_α has α-dependent units so that one cannot compare relative numerical values across different beads, nor can one perform any numerical computations (e.g., ensemble averaging of classifiers or cluster analysis). We return to this point momentarily. For now, we note

$$\Delta = 2dD_\alpha(n\tau)^\alpha = MSD_X(n\tau), \tag{7}$$

for any specific lag time $n\tau$, e.g., $n\tau = 0.1$ or 1 s, has units of μm^2 and, therefore, can be readily compared across multiple beads and used for averaging or cluster analysis. One can also use the GSER per bead and compare the dynamic moduli G' and G'' of different tracked beads at any frequency, e.g., 10 or 1 s^{-1}. *The potential problem with any of these single lag time or frequency projections onto a scalar quantity arises when the bead time series data have not been denoised first; indeed, the potential for error is exaggerated for the low-mobility, highly subdiffusive time series of beads inside flakes.* We illustrate this point below in Fig. 3, amplified further in the supplementary material. We perform cluster analysis on the classifiers of the primitive data (tracked bead time series), **not** on the GSER transform which is a nonlinear function of the primitive data.

In our approach, *the MSD classifier* $(\alpha,\ D_\alpha)$ *is a denoised projection onto fractional Brownian motion (fBm).* This classifier further provides *an analytical formula for the dynamic moduli surrounding each tracked bead* by virtue of the exact Fourier transform of any power-law MSD,

$$i\omega I\left(2dD_\alpha(n\tau)^\alpha\right) = \Gamma(1+\alpha)4D_\alpha\left(\frac{1}{\omega i}\right)^\alpha. \tag{8}$$

Using (8) in the GSER (3), the denoised classifier $(\alpha,\ D_\alpha)$ per individual bead yields an exact analytical formula for the local $G^*(\omega)$, thereby avoiding numerical error,

$$G^*(\omega) = \frac{k_BT\omega^\alpha}{\pi r\Gamma(1+\alpha)4D_\alpha}\left[\cos\left(\frac{\alpha\pi}{2}\right) + i\sin\left(\frac{\alpha\pi}{2}\right)\right] = G'(\omega) + iG''(\omega), \tag{9}$$

where $\Gamma(\cdot)$ is the Gamma function. From the ensemble of successfully denoised classifiers (α, D_α) per sample per bead diameter, we perform **three stages of clustering**. Since D_α has α-dependent fractional units to perform clustering, we either nondimensionalize D_α or project onto an appropriate scalar derived from the denoised classifier $(\alpha,\ D_\alpha)$.

The **first stage** is binary: *one cluster* of all tracked beads with a "waterlike" signal, which we define as a weakly subdiffusive signal consistent with tracking of beads in relatively dilute mucin solutions from the same experimental instrumentation (thus, likely *outside flakes*); *a second cluster* of tracked beads with a clear subdiffusive signal bounded away from waterlike signals (thus, likely *within flakes*).

The **second stage** is also binary, applied to the within-flake cluster. Bead increment time series are divided into those that *are, or are not, distinguishable from the noise floor of the experimental instrumentation*. The signature of the noise floor is achieved by tracking stationary beads glued to a glass plate with the experimental instrumentation, thereby identifying the classifier range where the signal is indistinguishable from the noise floor.

The **third stage** is the most intricate, consisting of **three levels of resolution** *applied independently to the successfully denoised outside- and within-flake clusters* from the above stages. Level 1: apply a homogeneity test to each cluster (Cochran's Q test [38,39]), and all clusters with sufficient data fail. Level 2: apply *a standard clustering algorithm* (MCLUST [40]) that yields clusters of "water like" and "within flake" denoised signals. Level 3: apply the homogeneity test to these refined (waterlike and within flake) clusters. We found that whenever there is sufficient data within clusters, they fail the test. These results guide the appropriate application of the GSER to *determine equilibrium dynamic moduli associated with the denoised clusters within the waterlike and flakelike ensembles*. This three-stage analysis of the experimental data yields several layers of heterogeneity in each progressive flake-burdened mucus sample, using the denoised classifier of particle mobility as the fundamental signal, and then the GSER to superimpose the associated heterogeneity in dynamic moduli.

Figure 2 illustrates the stages of this analysis *with synthetic simulated data* in the ideal scenario where *clusters* within flakes (middle panel) and outside flakes (left panel) *are homogeneous* and *constructed* from flakelike and dilute solution classifier data. By construction, the mixture is patently heterogeneous. In each panel, G' and G'' are computed using the GSER in three different ways: (1) applying GSER per bead using Eq. (9) with the denoised MSD classifier $(\alpha,\ D_\alpha)$, then ensemble averaging G' and G'' in frequency space; (2) ensemble averaging all denoised bead MSDs then applying GSER, Eq. (2); (3) ensemble averaging of the denoised MSD classifiers, giving a mean $(\alpha,\ D_\alpha)$, inserted into the GSER for fBm, Eq. (9). As noted earlier, averaging requires nondimensionalization of D_α or replacing it by one of the dimensional scalars derived from $(\alpha,\ D_\alpha)$, then ensemble averaging, then passing back to D_α.

The left and middle panels of Fig. 2 illustrate the *equivalence of using forms (1–3) of the GSER for synthetic homogeneous clusters*. The left panel data mimics waterlike signals from the dilute phase of HRM and the middle panel mimics flakelike signals from HRM, with a nondimensionalized version of classifier $(\alpha,\ D_\alpha)$, denoted as $(\alpha,\ \tilde{D}_\alpha)$, defined momentarily in Eq. (10), with each parameter drawn from independent normal distributions. For the waterlike signals, the means of $(\alpha,\ \tilde{D}_\alpha)$ are chosen

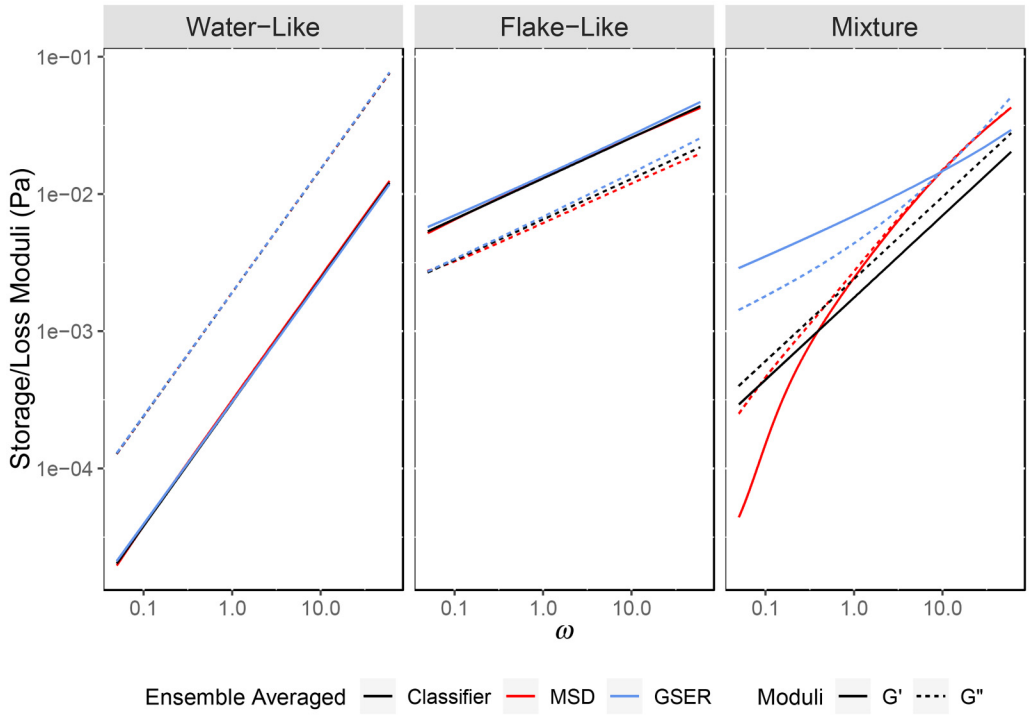

FIG. 2. Comparison between G' and G'' computed in three ways: (1) GSER applied to denoised MSD classifier (α, D_α) per bead, Eq. (9), then averaging G' and G'' in frequency space; (2) ensemble averaging over all denoised bead MSDs, then apply GSER, Eq. (2); (3) ensemble averaging of the denoised MSD classifiers, giving a mean (α, D_α), therefore, a denoised power law ensemble-average MSD, inserted into Eq. (9). These three approaches are implemented and shown to be equivalent for homogenous clusters: a waterlike homogeneous cluster in the left panel, cluster 1, a flakelike homogeneous cluster in the middle panel, cluster 2. Both left and middle panels illustrate consistency in all three approaches for homogeneous clusters. In stark contrast, the mean dynamic moduli of a heterogeneous mixture of these two clusters are computed with each approach in the right panel, illustrating inconsistency of the three approaches for heterogeneous mixtures.

$\mu = (0.9,\ 0.75)$ and their standard deviations are $\sigma = (0.03,\ 0.05)$. For the flakelike signals, the analogous means are $\mu = (0.3,\ 0.065)$ and standard deviations $\sigma = (0.07,\ 0.01)$. These synthetic clusters are homogeneous in the practical experimental sense of possessing a mean and standard deviation of parameters consistent with observed empirical data from homogeneous complex fluids. The standard deviation for α in the waterlike signal is constrained to be sufficiently small to avoid $\alpha > 1$ (and anomalous moduli).

The right-most panel *shows the nonequivalence of the three methods for averaging of tracked bead data in a heterogeneous two-phase mixture* synthetically created by simply combining these two normally distributed waterlike and flakelike clusters. Within each homogeneous cluster, all three approaches recover a power-law rheology scaling, i.e., approximately linear in the log-log space, whereas only approach (3) is mathematically guaranteed to do so. For the heterogeneous mixture in the right panel, methods (1) and (2) produce a non-power law scaling of G', G'', distinct from method (3).

Neither of the methods for the heterogeneous mixture in the right-most panel has meaningful physical relevance: they average over the underlying heterogeneity without knowledge of volume fractions of flakes and dilute solution and proper weighting of each in the average. If this additional information were experimentally accessible, and if we could assume passive interactions between flakes and nonflake solvent (which is completely unknown), one could infer linear microrheology of flake-burdened HRM that should, with sufficiently low stress-strain controls in a macrorheometer (e.g., cone and plate), agree with linear microrheology. We recall the local homogeneity assumption [41,42] of passive microrheology, i.e., that the dynamics of each particle is adequately described by a homogeneous complex fluid environment over the experimental timescale. This justifies the application of the GSER to each particle trajectory in order to estimate the local dynamic moduli of the fluid surrounding the particle being tracked [1–3,43,44]. The rheometric experiments used to validate the GSER theory for homogeneous fluids (e.g., [1,3]) are effectively averaging localized stress and strain in frequency sweeps over the full sample volume of the fluid; such dynamic moduli measurements are, we posit, consistent with the GSER averaging method (1), rather than the MSD averaging method (2) [or the corresponding model-based method (3)].

F. Data-analysis methods

Our strategy is to extract the pure stochastic fluctuation signal using an extension of the *fractional autoregressive moving average* (fARMA) denoising model developed in [18]. From [28], Fig. 3 below and in the section "The fARMAs Denoising Method" of the supplementary material, we show that *two extensions of the fARMA denoising procedure are necessary to accurately recover the pure,* i.e., *denoised signal* in simulated truth sets consistent with the

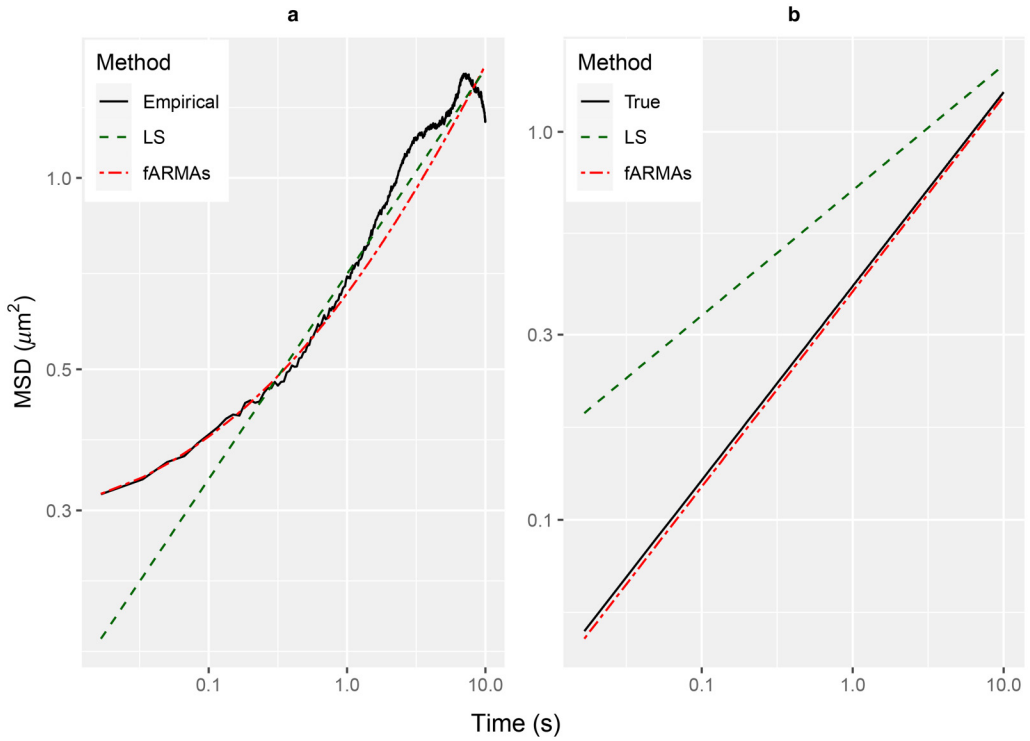

FIG. 3. (a) Empirical and fitted MSDs to simulated time series of fBm plus noise in the low signal-to-noise range. Fitted MSDs are from LS and fARMAs. N.B. fARMAs estimate the pure fBm signal plus high and low frequency noise, which together produce empirical MSD estimates. (b) LS and denoised fARMAs pure signal MSD estimates plus the pure signal MSD.

extremely low signal-to-noise-ratio (SNR) ranges of tracked beads within mucus flakes. First, fARMA is sensitive to the initial condition in the nonlinear optimization procedure. We resolve this hurdle with a least-squares predictor of the MSD followed by the fARMA corrector, which ensures a stable denoising procedure. Second, the inclusion of static noise in the fARMA model, which we call fARMAs, gives more accurate estimates of the pure signal in simulated truth data with low SNR. The Least-Squares predictor—fARMAs corrector method yields a two-parameter classifier for each tracked bead of the purely entropic, medium-induced, subdiffusive MSD over measured timescales. In Fig. 3 and more extensively Fig. S3 in the supplementary material, we illustrate the method on synthetic data, revealing estimators and standard errors across ranges of truth datasets generated from Brownian and subdiffusive processes, with superposition of various combinations of experimental error.

The standard method for estimating the dimensional MSD classifier parameters $(\alpha,\ D_\alpha)$ is via least-squares (LS), which consists of fitting the slope and intercept in the relation [45]

$$\log\left(MSD_X(n\tau)\right) = \log\left(2dD_\alpha\right) + \alpha \cdot \log\left(n\tau\right).$$

Since the empirical MSD is contaminated by noise at both the smallest (static and dynamic camera error) [46] and largest (drift of the sample) timescales [9,10], *lag times $n\tau$ in a restricted bandwidth are often used*. This approach does not remove the noise from the selected bandwidth: it merely assumes that noise contamination is negligible therein. However, this assumption is violated precisely in cases of interest here, for dense flakes, where the particle mobility is within or near the noise floor. To illustrate, Fig. 3(a) displays the MSD of fBm-contaminated by a noise floor of magnitude σ^2, for which the MSD is given by

$$MSD_{fBm+noise}(t) = 2dD_\alpha \cdot t^\alpha + 4 \cdot \sigma^2$$

and for which the corresponding signal-to-noise-ratio is $\mathrm{SNR} = (2dD_\alpha \cdot \tau^\alpha)/(4 \cdot \sigma^2)$. LS is fit to the bandwidth of 0.1–2 s, and we see that the line of best fit agrees very well with that of the empirical MSD over the bandwidth. However, this fit is to the MSD consisting of signal plus noise: Fig. 3(b) shows that the LS fit is very different from the MSD of the pure signal. In contrast, we employ an extension of the fARMA denoising model of [18] that includes static noise, denoted fARMAs [28], using the LS fit as a predictor step, which accurately recovers the pure signal in Fig. 3(b). Details of the fARMAs model and associated fitting procedure—including our predictor-corrector method—are given in the supplementary material.

From here on, we use the LS (predictor)—fARMAs (corrector) procedure (which we call fARMAs-PC) to estimate the diffusion parameters. The resulting *fractional-diffusion MSD classifier*, $(\alpha,\ D_\alpha)$, is estimated per tracked bead, then converted to be nondimensional or have comparable units [using (7) or Eq. (10) below] for quantitative analysis, in particular homogeneity testing and clustering.

III. A LITERATURE OVERVIEW OF HETEROGENEITY ANALYSIS

There is a considerable body of work in the microrheology literature on describing heterogeneity in fluids, much of which is reviewed in [47]. Qualitatively, heterogeneity is often measured via van Hove correlations (e.g., [12,48,49]). For given lag time $\Delta t = n\tau$, where τ is the minimum lagtime between particle position measurements, van Hove correlations compare the histogram of displacements $\Delta X(n\tau) = X(t + n\tau) - X(t)$ within and across particle trajectories to the Gaussian distribution theoretically expected for homogeneous fluids. A common finding is that the van Hove correlation in heterogeneous fluids is better fit by an exponential distribution than by a Gaussian (e.g., [12,48,49]), considered in [50] for *viscous* fluids with location-dependent diffusivity (e.g., [46–48]). However, the shape of the van Hove correlation function must be interpreted with extreme care at short timescales in our experiments and reconstituted HRM samples since the increments of low-mobility beads in flakes are strongly contaminated by the noise floor as shown in Fig. 3. Moreover, there is overwhelming evidence in our data that particles within flakes locally exhibit not viscous diffusion but strongly subdiffusive, viscoelastic dynamics (Fig. 4).

Quantitatively, heterogeneity is commonly measured using the excess kurtosis of the van Hove distribution at the given lagtime, or equivalently, the "non-Gaussianity" parameter (e.g., [51–53]),

$$\mathrm{NG}(n\tau) = \frac{\langle \Delta X(n\tau)^4 \rangle}{\langle 3\Delta X(n\tau)^3 \rangle} - 1.$$

Another metric is the heterogeneity ratio [54]

$$\mathrm{HR}(n\tau) = \frac{var(MSD_i(n\tau))}{mean(MSD_i(n\tau)^2)},$$

where $MSD_i(n\tau)$ is the MSD statistic (1) computed for particle i, for which efficient estimators of the ensemble mean and variance under the local homogeneity assumption are developed in [43]. Again, we remark that these calculations would need to be adjusted in the presence of noise floor contamination exhibited in Fig. 3.

For clustering of heterogeneous particle trajectories into homogeneous groups, Valentine *et al.* [48] develop a pairwise similarity metric between particle trajectories using the F-statistic

$$F_{i,j} = \frac{\sigma_i^2/N_i}{\sigma_j^2/N_j},$$

where σ_i and N_i are the standard deviation and number of the position increments $\Delta X_i(\tau)$ for particle i, and σ_j and N_j are defined analogously for particle j. Assuming that the increments are independently and identically normally distributed, $F_{i,j}$ follows an F distribution with (N_i, N_j) degrees of freedom if the dynamics of particles i and j are statistically indistinguishable [48]. uses the F-test to determine for each pair of particles whether or not they are statistically distinguishable at the 95% confidence level, which is then used to group the particles into clusters of indistinguishable members. However, the F-test assumes locally viscous dynamics. Moreover, it is not clear how to cluster particles when particle pairs (i, j) and (j, k) are both deemed indistinguishable, but pair (i, k) is not.

In light of these issues, Mellnik *et al.* [55], propose to cluster tracked particles via Gaussian mixture modeling, the approach we adopt here. Let $\hat{\theta}_i$ denote the estimate for bead trajectory i of its true classifier value θ_i. A simple choice of classifier is $\theta = (\alpha, \log \Delta)$, where $\Delta = MSD_{fBm}(t = 1\ s)$ via (7), with an in-depth discussion of various classifiers to follow. Given the classifiers of M trajectories, clustering is performed using the R

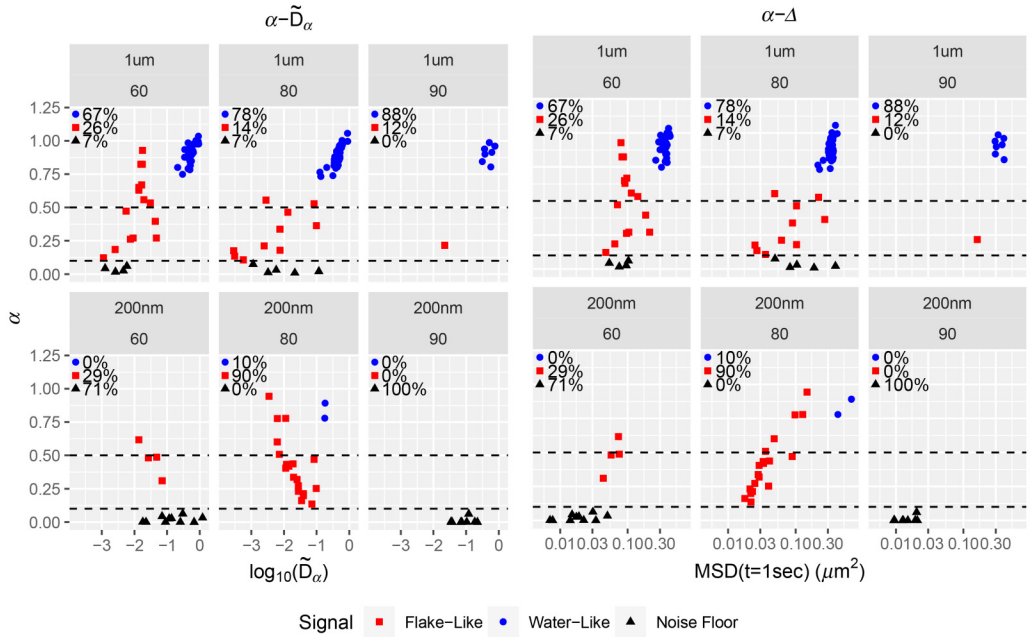

FIG. 4. $(a, \tilde{D}_a)$ (left) and (a, Δ) (right) classifier data for individual, 1 μm (top) and 200 nm (bottom) diameter beads in three different mucin mixtures. Classifier data are visually clustered into waterlike (circles), flakelike (squares), and noise floor (triangles) signals.

package MCLUST [42] using finite normal mixture models. That is, the classifier estimates $\hat{\theta}_1, \ldots, \hat{\theta}_M$ are clustered, in the most general case, according to the multivariate normal mixture model

$$J_i \overset{iid}{\sim} \text{Categorical}(\pi_1, \ldots, \pi_K),$$

$$\hat{\theta}_i \mid J_i \overset{iid}{\sim} \text{Normal}(\mu_{J_i}, \Sigma_{J_i}),$$

where K is the number of clusters and $J_i \in \{1, \ldots, K\}$ is the cluster to which particle i belongs. MCLUST estimates the posterior membership probability,

$$\hat{J}_i = \max_{1 \le k \le K} \Pr(J_i = k | \hat{\theta}_i, \hat{\Omega}),$$

where $\hat{\Omega}$ is the maximum likelihood estimate (MLE) of the clustering model parameters $\Omega = \{(\pi_k, \mu_k, \Sigma_k) : k = 1, \ldots, K\}$. MCLUST chooses K by fitting all models with $K \in \{1, \ldots, K_{max}\}$ for user-specified K_{max}, and selects the one with the lowest value of the Bayesian information criterion (BIC). It can also impose various constraints on the variance matrices, e.g., proportional variances $\Sigma_k = \tau_k \cdot \Sigma_0$ or diagonal variances $\Sigma_k = \text{diag}(\sigma^2_{k,1}, \ldots, \sigma^2_{k,K})$ (there are 14 possible variance restrictions in total, see Table 3 of [42]). This is particularly useful when some of the clusters are expected to consist of only a few particles, in which case the corresponding unconstrained variance matrices can be very poorly estimated. Once again, MCLUST estimates the posterior membership probabilities $\hat{J}_i$, $i = 1, \ldots, M$ from the best-fitting model (in terms of BIC) among all combinations of cluster sizes K and variance matrix constraints.

While the Gaussian mixture modeling algorithm of [55] is similar to ours, it differs in two key respects. For one, the algorithm of [55], determines the number of clusters using agglomerative clustering [56,57] with cutoff determined by the "gap statistic" method of [58], which is somewhat more involved than the BIC method described above. More importantly though, the algorithm of [55], clusters on standard deviation of the particle increments $\Delta X(n_*\tau)$ *for a single (but optimally chosen) lagtime* $\Delta t_* = n_*\tau$. In contrast, our clustering on the (denoised) classifier $\theta = (\alpha, \log \Delta)$ *leverages information from all experimental lagtimes*. This advantage was realized in [34,59], who employed the fBM classifier for heterogeneity assessment but did not pursue clustering of the classifier data.

IV. HOMOGENEITY TESTING

Now suppose that in addition to $\hat{\theta}_i$, for each trajectory i we have an estimate of the variance of the classifier, $V_i \approx \text{var}(\hat{\theta}_i)$. Such a variance estimator is obtained as a direct by-product of the fARMAs-PC denoising procedure. In order to test whether the $\hat{\theta}_1, \ldots, \hat{\theta}_M$ are obtained from a homogeneous cluster, let $Z_i = V_i^{-1/2}\hat{\theta}_i$ and $\bar{Z} = \frac{1}{M}\sum_{i=1}^{M} Z_i$. Then under the null hypothesis of homogeneity

$$H_0: \theta_1 = \cdots = \theta_M.$$

The so-called Cochran's Q statistic [22,38,39]

$$Q = \sum_{i=1}^{M} (Z_i - \bar{Z})^T (Z_i - \bar{Z})$$

has a $\chi^2_{p(M-1)}$ distribution under H_0, where p is the common number of elements of each $\hat{\theta}_i$, i.e., in our case we have $p = 2$. The assumption of homogeneity is then rejected at the ϵ level when $Q > C_\epsilon$, and C_ϵ is such that $\Pr\left(\chi^2_{p(M-1)} > C_\epsilon\right) = \epsilon$.

V. TRACKED PARTICLE CLASSIFIERS

A natural choice for the classifier of subdiffusive particle trajectories is $\theta = (\alpha, \log D_\alpha)$, where use of $\log D_\alpha$ reflects the empirical finding that D_α tends to vary by an order of magnitude within a given experimental setting, i.e., errors in fitting the slope extrapolate to fitting the y-intercept. However, the units of D_α are α-dependent, which precludes direct comparisons across beads. There are multiple ways to address this, e.g., one can simply evaluate the MSD at a chosen lag time $n\tau$, recall the discussion surrounding Eq. (7) above, which gives units of μm^2 for all beads, and thus admits inter-bead comparisons. A downside of this classifier is that the choice of MSD lag-time $n\tau$ is arbitrary, and one could have chosen any $n\tau$ to evaluate the MSD. Any clustering based on these arbitrary choices would have to be tested for robustness of the chosen timescale. We note, however, that if the ensemble data $(\alpha, \log D_\alpha)$ has been estimated by the fARMAs-PC method, then it has already used all of the denoised experimental data to produce the denoised classifier (α, D_α) for each bead, which produces a denoised power-law MSD estimate, and therefore the clustering outcome will be relatively robust for all choices of $MSD(n\tau)$.

This is not the case for standard LS-estimates of (α, D_α), illustrated in Fig. 3; namely, the LS estimates of MSD have different errors from the true signal MSD at every lag-time $n\tau$! An alternative approach to evaluation of MSD at lag-time $n\tau$ for some n is to nondimensionalize D_α, labelled $\tilde{D}_\alpha$. Once again, we emphasize that we use the fARMAs-PC method on the experimental data to produce the denoised classifier (α, D_α) for each bead. Using only experimental scales and a reference fluid relevant to mucus, *we define a power law* α-, *spatial dimension* d-, *and bead radius* r-*dependent rescaling of* D_α normalized with respect to the diffusivity of a bead of the same radius in water,

$$\tilde{D}_\alpha = \frac{d^{2(\alpha-1)} D_\alpha}{(D_w)^\alpha}, \tag{10}$$

where D_w is the viscous diffusivity of water for particles of

radius r. Note that,

$$\tilde{D}_\alpha = \frac{1}{(4r)^2} \cdot MSD(t = t^*),$$

where $t^* = (2r)^2/D_w$. In other words, $\tilde{D}_\alpha$ can be interpreted as a multiple of the MSD at a time t^* which depends on the particle radius r, instead of an experimental lag time $n\tau$. For 1 μm beads, $t^* = 2.33$ s, in the middle of the experimental lag times, and for 200 nm beads $t^* = 0.01$ s, just above the minimum experimental lag time τ. Of note, the homogeneity test produces identical results when applied to $(\alpha,\ \log\Delta)$ or $(\alpha,\ \log\tilde{D}_\alpha)$ since they are linear transformations of each other. The same is true for the MCLUST clustering algorithm with unconstrained variances.

The loss tangent as a scalar classifier:

For viscoelastic media, a fundamental property is that, instead of a scalar metric (viscosity for purely viscous, elasticity for purely solid, materials), the viscous and elastic moduli are functions of frequency. In this respect, a standard viscoelasticity metric is the loss tangent

$$\tan(\delta) = G''(\omega)/G'(\omega),$$

which *in general is frequency-dependent*. When $\delta > \pi/4$: $\tan(\delta) > 1$ *and the material is sol-like* (i.e., loss or viscosity dominated), whereas when $\delta < \pi/4$: $\tan(\delta) < 1$ *and the material is gel-like* (i.e., storage or elasticity dominated).

For pure power-law viscoelastic materials, $\tan(\delta)$ *collapses to a scalar function of the MSD power law exponent* α, *independent of both frequency* ω *and the MSD pre-factor* D_α. From the GSER (3) and the power-law moduli formulas (9),

$$\tan(\delta) = \frac{G''(\omega)}{G'(\omega)} = \tan\left(\frac{\pi\alpha}{2}\right), \tag{11}$$

giving $\delta = \frac{\pi\alpha}{2}$. Thus, *gel-like phases correspond to* $0 < \alpha < .5$ and *sol-like phases correspond to* $.5 < \alpha \leq 1$. This scalar classifier, see Fig. 5 below, is not as accurate as the two-parameter fBm classifier, $(\alpha,\ \tilde{D}_\alpha)$.

VI. RESULTS ON EXPERIMENTAL DATASETS

A. Coarse clustering: Beads within vs. outside flakes

Figure 4 gives the two-parameter classifier estimates for 1 μm and 200 nm diameter beads in three mucus mixtures: HBE + Calu3 60, 80, and 90 as described in the Materials and Data Collection. Two different scales are used for comparison: $(\alpha,\ \tilde{D}_\alpha)$ and $(\alpha,\ \Delta = MSD_X(t = 1\text{ s}))$. Recall that after taking logarithms of $\tilde{D}_\alpha$ and Δ, the two scales are linear transformations of each other. An advantage of using $\Delta = MSD_X(t = 1\text{ s})$ is that it allows for comparison between 1 μm and 200 nm beads, which cannot be done with $\tilde{D}_\alpha$ since it depends on bead diameter. *All datasets are visually divided into three clusters: waterlike or outside flakes, within flakes but entangled in the noise floor, and flakelike with recoverable signal.* The designation of tracked beads that are indistinguishable from the "noise floor" is based on a stuck bead analysis provided in the "Choosing a noise floor" section of the supplementary material with cutoff

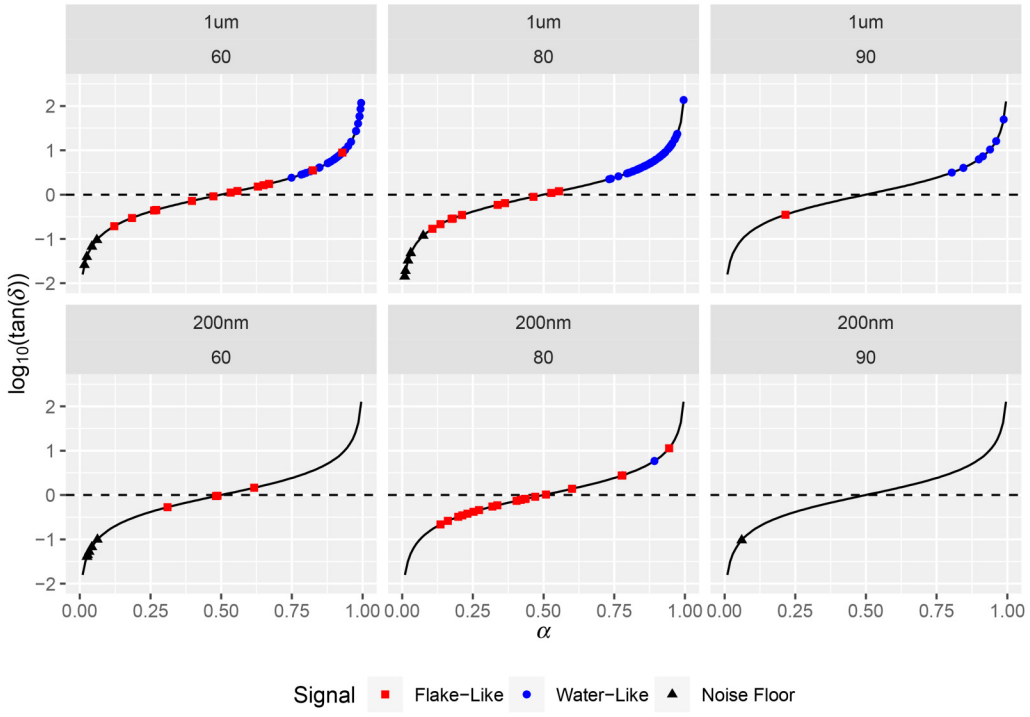

FIG. 5. $\log_{10}(\tan(\delta)) = \log_{10}[\tan(\alpha/2)]$ plots for 1 μm (left) and 200 nm (right) beads in HBE + Calu3 mucus samples 60, 80, and 90. Symbols (square, circle, triangle) correspond to the scalar loss tangent metric per bead, the solid curve is a plot of the function $\log_{10}(\tan(\alpha/2))$, and the dashed horizontal line signals the sol–gel boundary. Circles, squares, and triangles are from flakelike, waterlike, and noise floor clusters, respectively.

$\alpha < 0.1$. The flakelike data with recoverable pure signal exhibits significantly subdiffusive behavior yet above the noise floor. In [60], this classifier-based coarse clustering is shown, by comparison with visual data from all experimental datasets as in Fig. 1, to have extremely high accuracy in predicting beads within or at the periphery of flakes vs. outside flakes.

Figure 5 gives a visual equivalent of the $\alpha = 0.5$ cutoff in Fig. 4 as the separation between sol-like and gel-like local sample properties surrounding each bead. For easier graphical visibility, we plot $\log_{10}(\tan\delta)$, shifting the gel/sol cutoff in .. to 0, so that *positive values of* $\log_{10}(\tan\delta)$ *are sol-like and negative values gel-like*. All waterlike data is sol-like, all noise-floor data is gel-like, and all flakelike data lies between these extremes. We are interested especially in the percentage of sol-like and gel-like signals in flakelike data as a coarse scalar metric of heterogeneity. Use of $\tan\delta = 1$, equivalently $\alpha = 0.5$, as the sol-gel boundary is a fairly accurate predictor for waterlike vs. flakelike classification of tracked beads. It agrees with our two-parameter classifier for six of the eight samples. As could be expected in a phase separation process, two samples have overlapping α values above 0.5, and their cluster separation is only captured by using the two-parameter classifier as evidenced in Fig. 6 below. Formula (11) shows that using α as a scalar metric is equivalent to the loss tangent for power law fluids. Furthermore, our predictor-corrector method to infer (α, D_α) is extremely robust in estimation of α. Using only α as a classifier does a remarkably good job of predicting the clusters of beads within each sample, whereas D_α (upon converting to comparable units Δ or $\tilde{D}_\alpha$) basically plays the role of a corrector in singling out the few flakelike beads with values of α that could have been classified as waterlike. This coarse scalar metric does not, of course, convey the dynamic moduli surrounding each bead, and the reason to estimate (α, D_α) as accurately as possible. *We now proceed to two-parameter clustering and estimates of dynamic moduli, focusing on within-flake beads at 200 nm and 1* μm *diameter scales and tracking data distinguishable from the noise floor.*

B. Clustering analysis

Figure 6 displays the algorithmic *clustering results* obtained from MCLUST for *beads above the noise floor* ($\alpha > 0.1$) *and with a flakelike signal* for each of the two-dimensional classifiers: (i) $(\alpha, \log\Delta)$ and (ii) $(\alpha, \log\tilde{D}_\alpha)$. In both cases, the plotting axes are α vs. $\log\Delta$.

The top panel of Fig. 6 presents results for which the maximum number of clusters is set to $K_{max} = 2$, where both $(\alpha, \log\Delta)$ and $(\alpha, \log\tilde{D}_\alpha)$ classifiers return identical clustering. The bottom panel of Fig. 6 presents results for which the maximum number of clusters is set to $K_{max} = 4$, surmising there may be more than one or two distinguishable signals for flakelike beads.

The experiments with 1 μm diameter beads in 90% concentration and 200 nm diameter beads in 60% concentration contain too few beads above the noise floor to draw meaningful conclusions. The following observations apply to the remaining experiments.

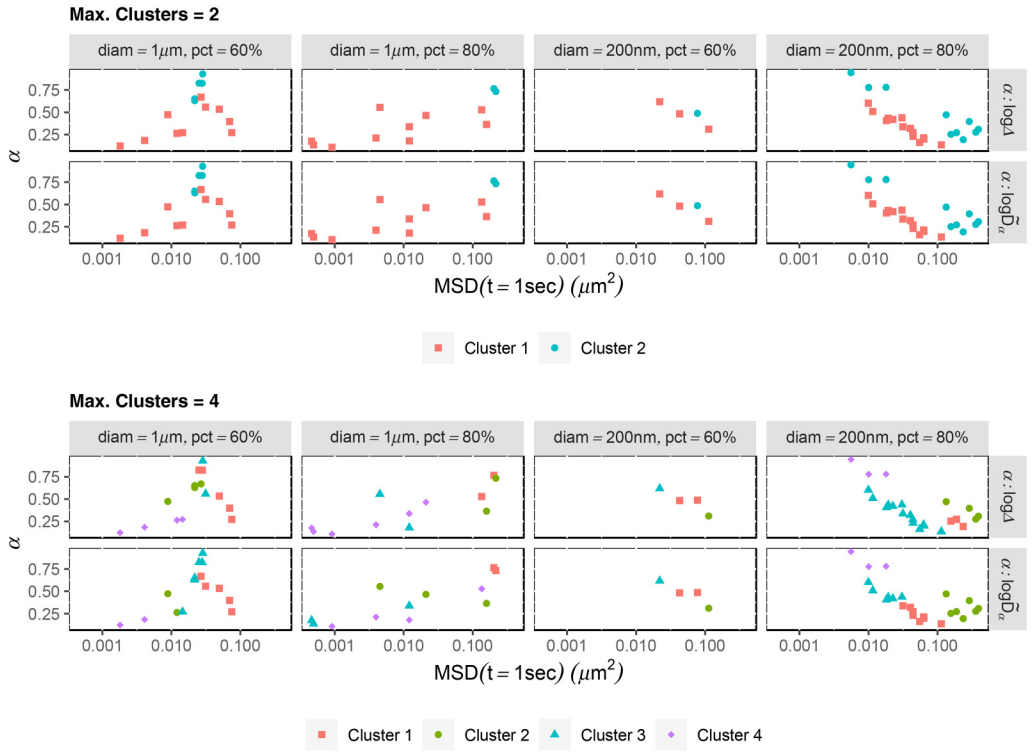

FIG. 6. Clustering results for classifiers $(\alpha, \log\Delta)$ and $(\alpha, \log\tilde{D}_\alpha)$ applied to all beads per sample above the noise floor with a flakelike signal, assuming a maximum of 2 clusters (top) and 4 clusters (bottom). The four samples with multiple beads are clustered using MCLUST. For each sample, the clustering results for each classifier are superimposed on the same set of particles, using the estimate of α on the vertical axis and the estimate of $\Delta = MSD(t = 1\ s)$ on the horizontal axis, in order to compare results for each sample and bead probe.

Overall, the two classifiers, $(\alpha,\ \log\Delta)$ and $(\alpha,\ \log\tilde{D}_\alpha)$, give similar results for distinguishing the highest and lowest mobility clusters, but differ in how they cluster the intermediate range data. This is because MCLUST has selected a constrained variance matrix, which is typically not invariant to the linear transformation between $(\alpha,\ \log\Delta)$ and $(\alpha,\ \log\tilde{D}_\alpha)$.

The BIC-based selection of the number of clusters employed by MCLUST picks more than two clusters for all four experiments. However, the MCLUST mixture-normal clustering approach struggles with nonelliptical clusters. That is, each of the K MCLUST clusters can be identified with an ellipse, and the data points belonging to it are those for which the "natural" distance to the ellipse centroid—i.e., along its principal axes and inversely proportional to the length of these axes—is smaller than for any other cluster's ellipse. This is why, e.g., the results with $K_{max} = 2$ for the 1 μm beads at 60% concentration may seem unexpected: while a visual clustering might separate the data points between left and right, MCLUST separates them between top and bottom because the small elliptical cluster at the top and large elliptical cluster at the bottom resulted in the smallest within-ellipse natural distance between data points and ellipse centroids.

The extent to which the visual clusters are not elliptical also explains why MCLUST typically selects more than two clusters, i.e., preferring to split highly nonelliptical clusters into several more elliptical ones. That being said, clusters corresponding to perfectly homogeneous particles according to the setup in the Homogeneity Testing section are indeed perfectly elliptical.

Taking all visual and algorithmic clustering results into account, we select a single clustering per experiment from the two panels of Fig. 6 summarized in Table I.

It should be noted that while $(\alpha,\ \log\Delta)$ is the chosen classifier for each of the five samples, for four out of the five samples, the $(\alpha,\ \log\tilde{D}_\alpha)$ classifier returns the same clusters.

C. Homogeneity testing within clusters

In order to assess within-cluster homogeneity, Table II presents the results of Cochran's Q test applied to each of the clusters of each experiment described in Table I, along with the cluster of beads with a waterlike signal.

All but five *p-values are extremely small* so that Cochran's Q test *strongly rejects cluster homogeneity*. The lack of homogeneity is expected for flakelike clusters as the data come from different flakes, each with pore structures arising from the stochastic phase separation process of flake formation. Furthermore, only one waterlike/outside-flake cluster passes a homogeneity test, and this is a weak conclusion since it is based on three beads. The outside-flake heterogeneity is also consistent with the stochastic dilution outside of phase-separated flakes, creating dilute phases that vary with relative proximity to flakes and degrees of dilution, with signals ranging from pure waterlike to varying mucin concentrations.

This determination of heterogeneity, both between and within the coarse within-flake and outside-flake bead signals, strongly supports the following **data-analysis protocol**: (1) for each batch sample, separately for subsamples with 200 nm and 1 μm beads, we use coarse clustering on the $(\alpha,\ \log\Delta)$ or $(\alpha,\ \log\tilde{D}_\alpha)$ classifier per bead to cluster beads within and outside of flakes; (2) when (here, both) clusters fail the homogeneity test, we further apply clustering to the within-flake and outside-flake ensembles; (3) for each cluster within and outside flakes, we apply the GSER with the denoised MSD for each bead; (4) for homogeneous clusters, either of the three methods illustrated in Fig. 2 can be used, while for heterogeneous clusters, we *average the dynamic moduli from all beads within each cluster*; (5) we assess cluster to cluster heterogeneity at the coarse scale of the within and outside-flake ensembles, and then at the finer scale of clusters within flakes and outside flakes. We refer to this data-analysis protocol for heterogeneous clusters as GSER average. These steps yield the within-flake and outside-flake dynamic moduli as revealed by 200 nm and 1 μm diameter probes, for each of the three reconstituted HBE samples, in Fig. 7. For comparison, Fig. 8 shows results using GSER average and the two alternative applications of the GSER, always applying the methods post clustering, namely, averaging within-cluster MSDs and then applying GSER, and averaging within-cluster classifiers and then applying GSER. As shown in the synthetic datasets in Fig. 2, the three methods yield equivalent results for homogeneous clusters but not for heterogeneous clusters.

TABLE I. Selected cluster assignment based on visual clustering and the algorithmic clustering results of Fig. 6. $K_{\max}$ refers to the max number of clusters, and K refers to the optimal number of clusters.

Diameter	HBE (%)	$K_{\max}$	K	Classifier
1 μm	60	2	2	$\alpha:\log\Delta$
1 μm	80	4	4	$\alpha:\log\Delta$
1 μm	90	2	2	$\alpha:\log\Delta$
200 nm	60	2	2	$\alpha:\log\Delta$
200 nm	80	4	4	$\alpha:\log\Delta$

TABLE II. Cochran's homogeneity test results for the clusters reported in Table I.

Diameter	HBE (%)	K	Group	No. beads	Q	P-value
1 μm	60	2	2	10	2688.6	0.0×10^{0}
		2	3	5	2.4	9.7×10^{-01}
		Waterlike	Waterlike	38	676.3	4.6×10^{-98}
	80	4	1	2	2.3	3.2×10^{-01}
		4	2	2	1.6	4.63×10^{-01}
		4	3	2	6.1	4.7×10^{-02}
		4	4	6	449.1	3.2×10^{-90}
		Waterlike	Waterlike	52	430.3	6.7×10^{-42}
	90	Waterlike	Waterlike	7	144.7	6.7×10^{-25}
200 nm	60	2	1	3	47.6	1.1×10^{-09}
		2	2	1	—	—
	80	4	1	3	5.6	2.3×10^{-01}
		4	2	4	58.0	1.1×10^{-10}
		4	3	14	1037.6	3.9×10^{-202}
		4	4	3	116.5	3.0×10^{-24}
		Waterlike	Waterlike	3	8.8	8.8×10^{-02}

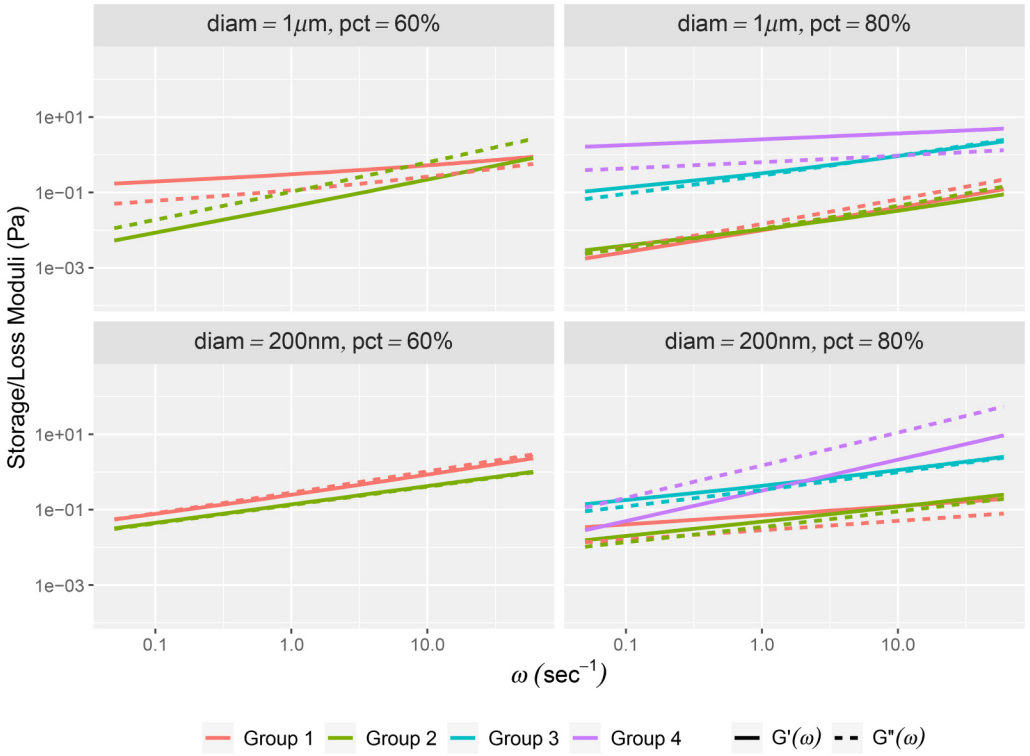

FIG. 7. Mean storage and loss moduli for each cluster in Table I using the "GSER Average" data-analysis protocol. Mean ± 2 s.d. intervals are included for all clusters consisting of at least two beads. Groups 1–4 are defined in Table II.

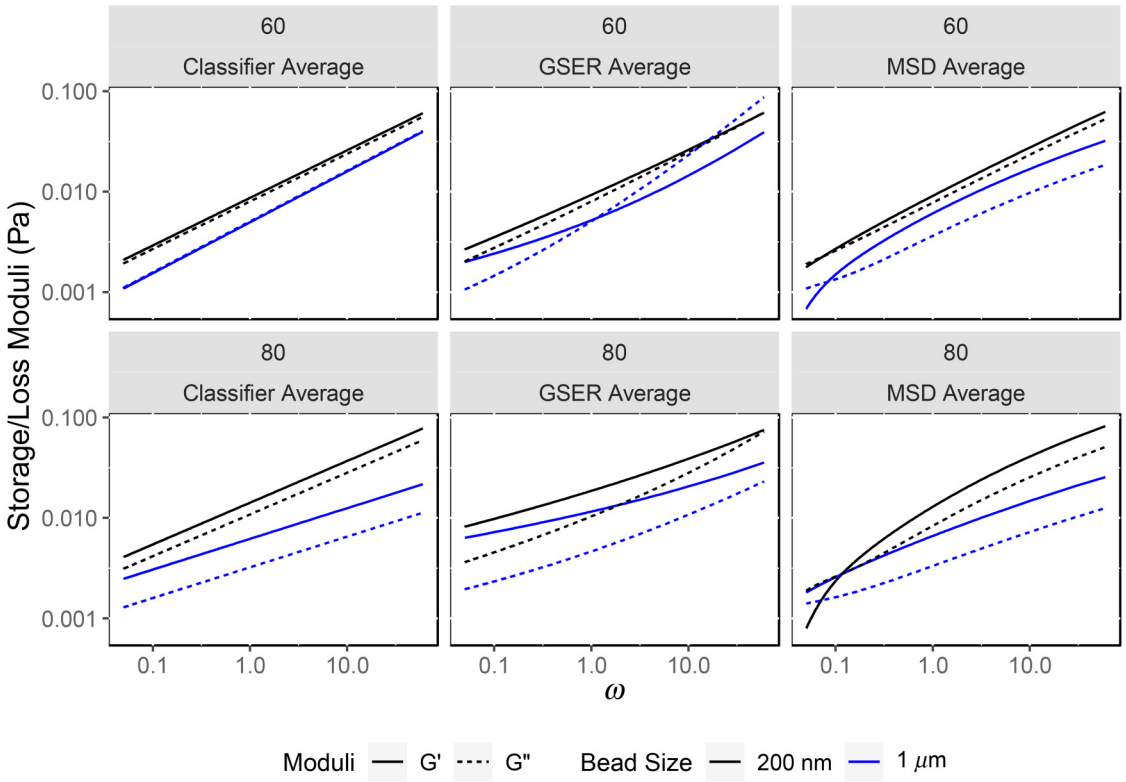

FIG. 8. Comparison of G′ (elastic) and G″ (viscous) moduli from 1 μm (gray) and 200 nm (black) tracked beads in the "flakelike" cluster for 60% (Row 1) and 80% (Row 2) samples, using the classifier average (Col. 1), the GSER average (Col. 2), and the MSD average (Col. 3). Only the GSER average (Col 2) results are justified due to inhomogeneity of the clusters.

D. Analysis of dynamic moduli

The storage and loss moduli for each cluster reported in Table I is displayed in Fig. 7, using the data-analysis protocol above. Since this involves weighted averages over power law functions ω^{α}, *there is a potential for within-flake and outside-flake sol–gel frequency transitions*. Due to evidence of heterogeneity in each cluster, we also display the mean ± two standard deviations of G' and G'' for each cluster in which there was more than one bead.

We find that for the 1 μm 60% reconstituted HRM sample, one within-flake cluster reflects a sol rheology and the other a gel rheology over all frequencies. The 200 nm 60% sample has clusters at the transition between gel-like and sol-like; one "cluster" contains a single bead and thus, there are no intervals around the moduli curves. These results comport with the stochastic phase separation process that produces flakes.

The 1 μm 80% reconstituted HRM sample shows two clusters with a sol rheology, one with a gel rheology once again hovering around the sol–gel transition. However, unlike the previously discussed sample, the cluster at the gel-sol boundary reflects a slight sol–gel transition as frequency increases. This cluster is the only one to reflect a sol–gel frequency transition. If one averages over the entire within-flake bead ensemble, again averaging in frequency space as the only justifiable average, Fig. 8, then a sol–gel transition arises due to a spectrum of beads conveying α above and below 0.5.

Figure 8 shows the dynamic moduli curves from all beads in the "flakelike" clusters for the 60% and 80% reconstituted HRM samples. Due to nonhomogeneity of the clusters, only (unjustifiable) ensemble averaging of classifiers gives a power law with linear scaling in log-linear coordinates, while both the (justifiable) GSER average and (unjustifiable) MSD average each display a departure from power-law scaling. *An important result of the justifiable GSER average method is the evidence of a sol–gel transition from the ensemble of probes within flakes.* While one can focus on details revealed in Fig. 8, it is difficult to make strong conclusions due to low tracked bead sample sizes and the underlying stochasticity of the phase separation process of flake formation.

VII. CONCLUDING REMARKS

Experiments and statistical methods are developed and applied to analyze particle-tracking data from reconstituted human respiratory mucus samples that replicate changes in the MUC5B/MUC5AC ratio characteristic of healthy and CF progression. This task of particle tracking to infer equilibrium rheological properties is challenging in highly heterogenous soft materials in general, and especially so with flake-burdened HRM where within-flake and outside-flake domains are a result of a stochastic, phase-separation process that has only recently received scientific attention and understanding (cf [20,61–63].). In our analysis, three levels of heterogeneity are identified and characterized from the tracked bead data: (1) a coarse binary scale of dense, phase-separated, mucus flakes and dilute solution of remaining mucins; (2) within flakes, a binary separation of dense domains where bead signals can vs. cannot be confidently disentangled from the experimental noise floor; and (3) in light of failed tests for homogeneity at both of the above levels, a more refined cluster analysis is applied to the ensembles of 200 nm and 1 μm diameter beads for all three reconstituted HRM samples.

For each tracked bead, we develop a *two-parameter classifier metric* (α, D_α), where α is the power law and D_α is the pre-factor of the mean-squared-displacement (MSD), *of the entire denoised experimental time series*. This fractional Brownian motion (fBm) classifier of the pure medium-induced signal for each tracked bead has been shown to be a robust statistical metric for passive particle tracking in HBE mucus (cf. [6,9–12,15–18]). For beads in flakes, however, previous statistical metrics for fitting fBm to increment time series data are inaccurate, illustrated herein with synthetic data of noisy bead time series representative of tracked beads in dense flakes.

The fBm classifier metric involves two steps, each utilizing the full bead time series. The first *predictor step* is based on a least-squares fit to the mean-squared-displacement of fBm, $MSD_X(n\tau) = 2dD_\alpha(n\tau)^\alpha$, where $n\tau$ are all experimental lag times and τ is the minimum lag time between recorded bead positions of the microscope. This yields an initial (α, D_α) predictor estimate, which stabilizes the *corrector step* using the fARMAs method initially developed in [18] and extended for this study in [28]. Our predictor-corrector method (fARMAs-PC) is shown to accurately recover the truth in synthetic data mimicking beads in flakes for which previous metrics fail, as well as all beads in dilute solution, i.e., outside flakes.

We next apply cluster analysis to assess heterogeneity in each of the three reconstituted samples of HRM reflected by each bead diameter. While the power law α is dimensionless, the MSD pre-factor D_α has fractional, α-dependent time units. We transform D_α for each bead to have either the same physical units or a common nondimensionalization. We show multiple ways to do this, each giving similar clustering results using a standard clustering algorithm. We emphasize that clustering is implemented on the denoised time series classifier of the data, i.e., on the primitive measured data. After each of the two stages of clustering is performed, the coarse in-flake vs. outside-flake scale and then within each of the coarse clusters, we test the homogeneity of the clusters. This test justifies use of either the single bead or ensemble-averaged GSER to infer dynamic moduli of all cluster scales and for each bead diameter. Clusters within and outside flakes invariably fail a homogeneity test, strongly supporting the rheology protocol for each identified cluster: application of GSER for each single bead, and then frequency-space averaging of G' and G'' over all beads in the cluster. This protocol gives the dynamic moduli of inside-flake and outside-flake clusters for each of the three samples from both bead diameters. We find that flakes possess both sol and gel domains while the remaining dilute mucin solution is sol-like, both nonhomogeneous, consistent with the stochastic phase-separation process generating the flake-burdened mucus samples.

The fBm classifier (α, D_α) has an additional advantage. For each individual tracked bead, the fBm classifier yields an exact power law for the mean-squared-displacement (MSD)

over the full range of experimental timescales. Furthermore, the Fourier transform of a power law function is also exact and a power law function, so the GSER applied to the classifier of each bead yields *an exact power-law formula for the complex modulus, $G^*(\omega)$ of the medium surrounding each denoised, tracked bead,* avoiding numerical approximation. Since all within-flake and outside-flake experimental clusters fail the test for homogeneity, within-cluster averaging is performed in the frequency-domain postapplication of the GSER to the denoised MSD for individual beads in each cluster. This results in a nonpower law rheology for each cluster either within dense mucin flakes or in the mucin-depleted dilute solvent. The within-flake data with both 200 nm and 1 μm diameter beads in samples from the same reconstituted batch also reveals *probe size-dependent heterogeneity*. Finally, we use the relative number of 200 nm vs. 1 μm diameter beads that enter and reside in flakes to *roughly estimate flake pore-size distributions to reside predominantly between 200 nm and 1* μm*, with an unknown, nonzero percentage of pores above 1* μm. Further experiments and analysis are necessary to more quantitatively estimate pore-size distributions.

Novel contributions in this paper

Our goal in this paper is a treatment of heterogeneous soft materials through the use of particle-tracking microrheology that theorists and experimentalists may adopt in their work. We describe novel experimental results by Papanikolas and Freeman on synthetic replication of flake-endowed mucus that will be the focus of an upcoming separate submission, whereas the primary focus and novelty of this paper are our analysis of the experimental particle-tracking data to characterize heterogeneity of the reconstituted mucus samples. The analytical methods clarify what is possible to infer about rheological heterogeneity of the samples from the data, and, therefore, the methods are adaptable to other materials and data. We demonstrate the ability to replicate empirical MSDs with the method presented herein, fARMAs-PC. To do so, *we simulate homogeneous flakelike datasets and dilute-solutionlike datasets* and recover the known truth with our methods applied to the simulated datasets. We then show all averaging GSER methods are quantitatively equivalent. It is well known that ensemble-averaging of tracked bead MSDs is the proper approach for a homogeneous complex fluid. In our samples and analyses, the data are heterogeneous (determined by homogeneity tests and clustering with MCLUST). Therefore, ensemble-averaging MSDs in the GSER is patently a violation of the theory. Further, we show *each tracked bead trajectory that can be distinguished from the experimental noise floor robustly obeys a unique fBm stochastic process*. The data, therefore, strongly supports that every successfully denoised tracked bead resides in a locally homogeneous medium over the full timescales and lengthscale of every tracked bead, supported by 1800 position observations, and the medium is conveying a memory spectrum consistent with a unique fBm process as uniquely determined by our classifier. These results support application of the single-particle GSER formula to infer the loss and storage moduli of the medium surrounding each tracked bead. From the ensembles of tracked and denoised beads per sample and bead size, we determine whether the ensembles are drawn from a homogeneous distribution of fBm processes or not.

If the ensemble is not homogeneous, averaging in frequency space is the only justifiable analysis of the data, as ensemble-averaging of MSDs violates the original GSER theory. If the ensemble is homogeneous, all GSER methods are equivalent, which we show quite demonstrably with simulated data consistent with the experimental datasets.

SUPPLEMENTARY MATERIAL

See the supplementary material for (1) explanation of our denoising method, fARMAs-PC, that is applied to all tracked bead position time series. (2) Explanation of our parameter estimation method that provides the fractional Brownian motion classifier consisting of two parameters, (α, D_α). (3) Explanation of how we measured the noise floor threshold in the 2-parameter space (α, D_α) derived from beads stuck to the glass plate, with results from stuck bead data in Fig. S1. (4) Illustration of convergence results from our predictor-corrector method to estimate the classifier, noise, and drift parameters in Fig. S2. (5) Comparison of our predictor-corrector method vs. the LS method for estimating the classifier parameters (α, D_α), where the methods are applied to simulated truth sets where the correct parameters are known, Fig. S3. (6) Discussion of data cleaning methods and the results of filtered data for each reconstituted mucus sample and each tracked bead diameter. (7) Illustration of how our methods applied to experimental and synthetic datasets provide an accurate reconstruction of the empirical MSDs of tracked beads, Figs. S4 and S5.

ACKNOWLEDGMENTS

Partial financial support for this work is provided by the Natural Sciences and Engineering Research Council of Canada (No. RGPIN-2020-04364) for M.L., NSF (No. CISE-1931516) for M.G.F., the Sloan Foundation (No. G-2021-14197) for M.P., R.F., and M.G.F., the Cystic Fibrosis Foundation (No. FREEMA19G0) for M.P. and R.F., the Cystic Fibrosis Foundation (Nos. HILL19G0, HILL20y2-OUT, and BOUCHE19R0), and the National Institutes of Health (Nos. P30DK065988 and 1P01HL164320) for D.B.H. and M.M.

AUTHOR DECLARATIONS

Conflict of Interest

The authors have no conflicts to disclose.

DATA AVAILABILITY

The data that support the findings of this study are available from the corresponding authors upon reasonable request.

REFERENCES

[1] Mason, T. G., and D. A. Weitz, "Optical measurements of frequency-dependent linear viscoelastic moduli of complex fluids," Phys. Rev. Lett. **74**, 1250–1253 (1995).

[2] Mason, T. G., K. Ganesan, J. H. van Zanten, D. Wirtz, and S. C. Kuo, "Particle tracking microrheology of complex fluids," Phys. Rev. Lett. **79**, 3282–3285 (1997).

[3] Mason, T. G., "Estimating the viscoelastic moduli of complex fluids using the generalized Stokes-Einstein equation," Rheol. Acta **39**, 371–378 (2000).

[4] Squires, T. M., and T. G. Mason, "Fluid mechanics of microrheology," Annu. Rev. Fluid Mech. **42**, 413–438 (2010).

[5] Fahy, J. V., and B. F. Dickey, "Airway mucus function and dysfunction," N. Engl. J. Med. **363**(23), 2233–2247 (2010).

[6] Bansil, R., and B. S. Turner, "The biology of mucus: Composition, synthesis and organization," Adv. Drug Delivery Rev. **124**, 3–15 (2018).

[7] Wagner, C. E., K. M. Wheeler, and K. Ribbeck, "Mucins and their role in shaping the functions of mucus barriers," Annu. Rev. Cell Dev. Biol. **34**, 189–215 (2018).

[8] Boucher, R. C., "Muco-obstructive lung diseases," N. Engl. J. Med. **380**, 1941–1953 (2019).

[9] Crater, J. S., and R. L. Carrier, "Barrier properties of gastrointestinal mucus to nanoparticle transport," Macromol. Biosci. **10**(12), 1473–1483 (2010).

[10] Hill, D. B., P. A. Vasquez, J. Mellnik, S. A. McKinley, A. Vose, F. Mu, A. G. Henderson, S. H. Donaldson, N. E. Alexis, R. C. Boucher, and M. G. Forest, "A biophysical basis for mucus solids concentration (wt%) as a candidate biomarker for airways disease: Relationships to clearance in health and stasis in disease," PLoS One **9**(2), e87681 (2014).

[11] Lysy, M., N. Pillai, D. B. Hill, M. G. Forest, J. Mellnik, P. Vasquez, and S. A. McKinley, "Model comparison and assessment for single particle tracking in biological fluids," J. Am. Stat. Assoc. **111**(516), 1413–1426 (2016).

[12] Wagner, C. E., B. S. Turner, M. Rubinstein, G. H. McKinley, and K. Ribbeck, "A rheological study of the association and dynamics of MUC5AC gels," Biomacromolecules **18**(11), 3654–3664 (2017).

[13] Thapa, S., M. A. Lomholt, J. Krog, A. G. Cherstvy, and R. Metzler, "Bayesian analysis of single-particle tracking data using the nested-sampling algorithm: Maximum-likelihood model selection applied to stochastic-diffusivity data," Phys. Chem. Chem. Phys. **20**(46), 29018–29037 (2018).

[14] Hill, D. B., R. Long, W. Kissner, E. Atieh, I. Garbarine, M. Markovetz, N. Fontana, M. Christy, M. Habibpour, R. Tarran, M. G. Forest, R. Boucher, and B. Button, "Pathological mucus and impaired mucus clearance in cystic fibrosis patients results from increased concentration, not altered pH," Eur. Respir. J. **52**(6), 1801297 (2018).

[15] Newby, J., A. Schaefer, P. Lee, M. G. Forest, and S. Lai, "Convolutional neural networks automate detection for tracking of submicron scale particles in 2D and 3D," Proc. Natl. Acad. Sci. U.S.A. **115**(36), 9026–9031 (2018).

[16] Esther, C., M. Muhlebach, C. Ehre, D.B. Hill, M. Wolfgang, M. Kesimer, K. Ramsey, M. Markovetz, I. Garbarine, M.G. Forest, I. Seim, B. Zorn, C. Morrison, M. Delion, W. Thelin, D. Villalon, J. R. Sabater, L. Turkovic, S. Ranganathan, S Stick, S. Conlan, R. Boucher, "Mucus accumulation in the lungs precedes structural changes and infection in children with cystic fibrosis," Sci. Transl. Med. **11**(486), eaav3488 (2019).

[17] Markovetz, M. R., C. R. Esther Jr, M. S. Muhlebach, M. J. Papanikolas, R. Freeman, X. Cao, M. G. Forest, and D. B. Hill, "Establishing the mucus flake burden as a biomarker of CF disease severity," Pediatr. Pulmonol. **54**(S2), S161 (2019).

[18] Ling, Y., M. Lysy, I. Seim, J. Newby, D. Hill, J. Cribb, and M. G. Forest, "Measurement error correction in particle tracking microrheology," Ann. Appl. Stat. **16**(3), 1747–1773 (2022).

[19] Valentine, M. T., Z. E. Perlman, M. L. Gardel, J. H. Shin, P. Matsudaira, T. J. Mitchison, and D. A. Weitz, "Colloid surface chemistry critically affects multiple particle tracking measurements of biomaterials," Biophys. J. **86**(6), 4004–4014 (2004).

[20] Ford, A. G., X. Cao, M. J. Papanikolas, T. Kato, R. C. Boucher, M. R. Markovetz, D. B. Hill, R. Freeman, and M. G. Forest, "Molecular dynamics simulations to explore the structure and rheological properties of normal and hyper-concentrated airway mucus," Stud. Appl. Math. **147**(4), 1369–1387 (2021).

[21] Markovetz, M., I. C. Garbarine, C. B. Morrison, W. J. Kissner, I. Seim, M. G. Forest, M. J. Papanikolas, R. Freeman, A. Ceppe, A. Ghio, N. E. Alexis, S. M. Stick, C. Ehre, R. C. Boucher, C. R. Esther, M. S. Muhlebach, and D. B. Hill, "Mucus and mucus flake composition as candidate biomarkers of CF airway disease progression," J. Cystic Fibrosis **21**(6), 959–966 (2022).

[22] Zhang, K., K. Crizer, M. Schoenfisch, D. B. Hill, and G. Didier, "Fluid heterogeneity detection based on the asymptotic distribution of the time-averaged mean squared displacement in single particle tracking experiments," J. Phys. A: Math. Theor. **51**, 445601 (2018).

[23] Sikora, G., K. Burnecki, and A. Wyłomańska, "Mean-squared-displacement statistical test for fractional Brownian motion," Phys. Rev. E **95**, 032110 (2017).

[24] Batson, B. D., B. T. Zorn, G. Radicioni, S. S. Livengood, T. Kumagai, H. Dang, A. Ceppe, P. W. Clapp, M. Tunney, J. S. Elborn, N. G. McElvaney, M. S. Muhlebach, R. C. Boucher, M. Tiemeyer, M. C. Wolfgang, and M. Kesimer, "Cystic fibrosis airway mucus hyperconcentration produces a vicious cycle of mucin, pathogen, and inflammatory interactions that promotes disease persistence," Am. J. Respir. Cell Mol. Biol. **67**(2), 253–265 (2022).

[25] Levine, A. J., and T. C. Lubensky, "One- and two-particle microrheology," Phys. Rev. Lett. **85**, 1774–1777 (2000).

[26] Hohenegger, C., and M. G. Forest, "Two-point microrheology: Modeling protocols," Phys. Rev. E **78**, 031501 (2008).

[27] Crocker, J. C., M. T. Valentine, E. R. Weeks, T. Gisler, P. D. Kaplan, A. G. Yodh, and D. A. Weitz, "Two-point microrheology of inhomogeneous soft materials," Phys. Rev. Lett. **85**, 888–891 (2000).

[28] Caughman, N., Data analysis and material property inferences from passive microbead rheology experiments in heterogeneous biological systems, PhD dissertation, UNC Chapel Hill, 2023.

[29] Kesimer, M., C. Ehre, C. W. Davis, J. K. Sheehan, and R. J. Pickles, "Molecular organization of the mucins and glycocalyx underlying mucus transport over mucosal surfaces of the airways," Mucosal Immunol. **6**, 379–392 (2013).

[30] Hill, D. B., and B. Button, "Establishment of respiratory air-liquid interface cultures and their use in studying mucin production, secretion, and function," Methods Mol. Biol. **842**, 245–258 (2012).

[31] Kesimer, M., S. Kirkham, R. J. Pickles, A. G. Henderson, N. E. Alexis, G. Demaria, D. Knight, D. J. Thornton, and J. K. Sheehan, "Tracheobronchial air-liquid interface cell culture: A model for innate mucosal defense of the upper airways?," Am. J. Physiol. Lung Cell Mol. Physiol. **296**(1), L92–L100 (2009).

[32] Wagner C. E., M. Krupkin, K. B. Smith-Dupont, C. M. Wu, N. A. Bustos, J. Witten, and K. Ribbeck, "Comparison of physicochemical properties of native mucus and reconstituted mucin gels," Biomacromolecules **24**(2), 628–639 (2023).

[33] Carpenter, J., Y. Wang, R. Gupta, Y. Li, P. Haridass, D. B. Subramani, B. Reidel, L. Morton, C. Ridley, W. K. O'Neal, M. P. Buisine, C. Ehre, D. J. Thornton, and M. Kesimer, "Assembly and organization of the N-terminal region of mucin MUC5AC: Indications for structural and functional distinction from MUC5B," Proc. Natl. Acad. Sci. U.S.A. **118**, e2104490118 (2021).

[34] Duits, M. H., Y. Li, S. A. Vanapalli, and F. Mugele, "Mapping of spatiotemporal heterogeneous particle dynamics in living cells," Phys. Rev. E **79**(5 Part 1), 051910 (2009).

[35] Allan, D. B., T. Caswell, N. C. Keim, C. M. van der Wel, and R. W. Verweij, (2024). soft-matter/trackpy: v0.6.3rc1 (v0.6.3rc1). Zenodo.

[36] Backlund, M., and W. E. Moerner, "Motion of chromosomal loci and the mean-squared displacement of a fractional Brownian motion in the presence of static and dynamic errors," Proc. SPIE **9331**, 933106 (2015).

[37] Backlund, M., R. Joyner, and W. E. Moerner, "Chromosomal locus tracking with proper accounting of static and dynamic errors," Phys. Rev. E **91**, 062716 (2015).

[38] Cochran, W. G., "Problems arising in the analysis of a series of similar experiments," J. R. Stat. Soc. Suppl. **4**, 102–118 (1937).

[39] Cochran, W. G., "The combination of estimates from different experiments," Biometrics **10**, 101 (1954).

[40] Scrucca, L., M. Fop, T. B. Murphy, and A. E. Raftery, "MCLUST 5: Clustering, classification and density estimation using Gaussian finite mixture models," R J. **8**(1), 289 (2016).

[41] Savin, T., and P. S. Doyle, "Statistical and sampling issues when using multiple particle tracking," Phys. Rev. E **76**(2 Pt 1), 021501 (2007).

[42] Kumar, P., J. Tamayo, R Shiu, W. Chin, and A. Gopinath, "Size-dependent diffusion and dispersion of particles in mucin," Polymers **15**(15), 3241 (2023).

[43] Kubo, R., "The fluctuation-dissipation theorem," Rep. Prog. Phys. **29**(1), 255–284 (1966).

[44] Zwanzig, R., *Nonequilibrium Statistical Mechanics* (Oxford University, New York, 2001).

[45] Didier, G., and K. Zhang, "The asymptotic distribution of the pathwise mean squared displacement in single particle tracking experiments," J. Time Ser. Anal. **38**(3), 395–416 (2016).

[46] Savin, T., and P. Doyle, "Static and dynamic errors in particle tracking microrheology," Biophys. J. **88**(1), 623–638 (2005).

[47] Rose, K. A., M. Molaei, M. J. Boyle, D. Lee, J. C. Crocker, and R. J. Composto, "Particle tracking of nanoparticles in soft matter," J. Appl. Phys. **127**(19), 191101 (2020).

[48] Valentine, M. T., P. D. Kaplan, D. Thota, J. C. Crocker, T. Gisler, R. K. Prud'homme, M. Beck, and D. A. Weitz, "Investigating the microenvironments of inhomogeneous soft materials with multiple particle tracking," Phys. Rev. E **64**(6), 061506 (2001).

[49] Scott, S., M. Weiss, C. Selhuber-Unkel, Y. F. Barooji, A. Sabri, J. T. Erler, R. Metzler, and L. B. Oddershede, "Extracting, quantifying, and comparing dynamical and biomechanical properties of living matter through single particle tracking," Phys. Chem. Chem. Phys. **25**(3), 1513–1537 (2023).

[50] Wang, B., J. Kuo, S. C. Bae, and S. Granick, "When Brownian diffusion is not Gaussian," Nat. Mater. **11**, 481–485 (2012).

[51] Rahman, A., "Correlations in the motion of atoms in liquid argon," Phys. Rev. **136**(2A), A405–A411 (1964).

[52] Nijboer, B. R. A., and A. Rahman, "Time expansion of correlation functions and the theory of slow neutron scattering," Physica **32**(2), 415–432 (1966).

[53] Kegel, W. K., and A. van Blaaderen, "Direct observation of dynamical heterogeneities in colloidal hard-sphere suspensions," Science **287**, 290–293 (2000).

[54] Rich, J. P., G. H. McKinley, and P. S. Doyle, "Size dependence of microprobe dynamics during gelation of a discotic colloidal clay," J. Rheol. **55**(2), 273–299 (2011).

[55] Mellnik, J., P. A. Vasquez, S. A. McKinley, J. Witten, D. B. Hill, and M. G. Forest, "Micro-heterogeneity metrics for diffusion in soft matter," Soft Matter **10**(39), 7781–7796 (2014).

[56] Ward, J. H., "Hierarchical grouping to optimize an objective function," J. Am. Stat. Assoc. **58**(301), 236–244 (1963).

[57] Johnson, S. C., "Hierarchical clustering schemes," Psychometrika **32**, 241–254 (1967).

[58] Tibshirani, R., G. Walther, and T. Hastie, "Estimating the number of clusters in a data set via the gap statistic," J. R. Stat. Soc. B **63**(2), 411–423 (2001).

[59] Esther, C. R., Jr., M. S. Muhlebach, C. Ehre, D. B. Hill, M. C. Wolfgang, M. Kesimer, K. A. Ramsey, M. R. Markovetz, I. C. Garbarine, M. G. Forest, I. Seim, B. Zorn, C. B. Morrison, M. F. Delion, W. R. Thelin, D. Villalon, J. R. Sabater, L. Turkovic, S. Ranganathan, S. M. Stick, and R. C. Boucher, "Mucus accumulation in the lungs precedes structural changes and infection in children with cystic fibrosis," Sci. Transl. Med. **11**, eaav3488 (2019).

[60] Kass, R. E., and A. E. Raftery, "Bayes factors," J. Am. Stat. Assoc. **90**(430), 791 (1995).

[61] Henderson, A. G., C. Ehre, B. Button, L. H. Abdullah, L. H. Cai, M. W. Leigh, G. C. DeMaria, H. Matsui, S. H. Donaldson, C. W. Davis, J. K. Sheehan, R. C. Boucher, and M. Kesimer, "Cystic fibrosis airway secretions exhibit mucin hyperconcentration and increased osmotic pressure," J. Clin. Invest. **124**(7), 3047–3060 (2014).

[62] Vasquez, P., B. Walker, K. Bloom, D. Kolbin, N. Caughman, R. Freeman, M. Lysy, C. Hult, K. A. Newhall, M. Papanikolas, C. Edelmaier, and M. G. Forest, "The power of weak, transient interactions across biology: A paradigm of emergent behavior," Phys. D **454**, 133866 (2023).

[63] Crocker, J. C., and B. D. Hoffman, "Multiple-particle tracking and two-point microrheology in cells," Methods Cell Biol. **83**, 141–178 (2007).